Measured and calculated radiative lifetime and optical absorption of $In_xGa_{1-x}N$/GaN quantum structures

E. Berkowicz, D. Gershoni, and G. Bahir
The Solid State Institute, Technion-Israel Institute of Technology, Haifa 32000, Israel

E. Lakin, D. Shilo, and E. Zolotoyabko
Department of Materials Engineering, Technion-Israel Institute of Technology, Haifa 32000, Israel

A. C. Abare, S. P. Denbaars, and L. A. Coldren
Department of Electrical and Computer Engineering University of California, Santa Barbara, California 93106

(Received 8 September 1999; revised manuscript received 6 December 1999)

We apply photoluminescence, photoluminescence excitation, and time-resolved optical spectroscopy for studying a set of $In_xGa_{1-x}N$/GaN periodic structures, which were characterized by high-resolution x-ray diffraction including x-ray mapping in reciprocal space. We found that the energy differences between the absorption edge and the photoluminescence peak (Stokes shift), and the photoluminescence decay time drastically increase with the $In_xGa_{1-x}N$ layer thickness. The decay time strongly increases with the sample temperature. We were able to quite accurately determine the radiative and nonradiative decay times of excitons in these structures by measuring the temperature dependence of the decay times, the integrated photoluminescence intensities, and the photoluminescence intensities immediately after the picosecond excitation pulse. The intrinsic radiative lifetimes, which are inversely proportional to the exciton oscillator strengths, were then calculated from the temperature dependence of the radiative lifetimes. These experimental findings are analyzed using an eight-band $\mathbf{k}\cdot\mathbf{P}$ model, which quantitatively explains both the Stokes shifts and the intrinsic radiative lifetimes. Their strong dependence on the quantum well width is due to a large ($\sim$1 MV/cm) lattice-mismatch strain-induced piezoelectric field along the growth axis.

I. INTRODUCTION

Considerable progress in the heteroepitaxy of group-III nitrides using low-temperature-deposited buffer layers[1–3] have recently led to the demonstration of new devices operating in the UV spectral range. In most of these light-emitting diodes and laser diodes, $In_xGa_{1-x}N$ quantum-well (QW) layers embedded within GaN barrier layers are acting as the active layers.[4] Therefore, the electronic and optical properties of this material system have become a subject of intensive research efforts. Key issues in these studies are (i) the value of the optical band gap and its composition and strain dependence, (ii) the reason for the large difference between the absorption and the emission spectrum (Stokes shift), and (iii) the recombination dynamics of excitons and free carriers in these heterostructures. The studies of the optical properties of this technologically important material system are interesting and quite complicated for interpretation due to its unique properties. For example, the presence of large lattice mismatch-induced strain fields in these heterostructures is reported to lead to the presence of strong piezoelectric fields. In addition, the presence of large density of dislocations, interface roughness, composition fluctuations, and in some cases even regions of a complete phase separation are also reported.[5,6] These are unavoidably affecting the optical properties of the heterostructures. Consequently, it is not straightforward to characterize and to correctly interpret their optical properties, since various intrinsic and extrinsic physical phenomena must be carefully considered in the analysis of the experimental data. For example, potential fluctuations due to composition fluctuations have been invoked in order to explain the observation of a large energy difference between the band-edge absorption and emission (Stokes shift).[7] Other researchers suggested three dimensional carriers localization and the possible formation of quantum dots due to a complete phase separation within the strained $In_xGa_{1-x}N$ layers.[8] In contrast, recent reports have raised the importance of the quantum-confined Stark effect[9] due to the piezoelectric fields in the strained wurtzite-type nitride compound quantum wells (QWs).[10–16]

In this work we report on (cw) and pulsed optical spectroscopy studies of a set of $In_xGa_{1-x}N$/GaN multiple-quantum-well (MQW) samples. We first characterize these samples by high-resolution x-ray-diffraction (HRXRD) measurements, by which their composition and layer thicknesses and the amount of strain relaxation were determined. The samples which have various $In_xGa_{1-x}N$ QW widths (d_w), but same In content (x) and same barrier width (d_b), were then investigated optically. We applied, in a complementary way, temperature-dependent photoluminescence (PL), PL decay time measurements, PL excitation (PLE), and time-resolved PL spectroscopy. Our experimental findings were then analyzed by an eight-band $\mathbf{k}\cdot\mathbf{P}$ model[17,18] that we modified in order to take into account the hexagonal symmetry of this system.[19] This detailed model is required, in order to correctly consider the complexity of the valence-band structure in these strained quantum heterostructures. The model quantitatively explains both the cw and the pulsed measurements and their temperature and well width dependence. The strong dependence on the QW width is explained in terms of

 ©2000 The American Physical Society

a strong lattice-mismatch strain-induced piezoelectric field along the growth axis.

The paper is organized as follows: In Sec. II we describe the samples, their growth procedure and x-ray characterizations. In Sec. III we discuss the theoretical eight-band $\mathbf{k}\cdot\mathbf{P}$ model which we use for simulating the optical properties of these quantum structures. In Sec. IV we present the optical measurements, and in Sec. V these measurements are analyzed and discussed. The paper includes two appendixes. Appendix A outlines the theoretical background of reciprocal space mapping applied to heterostructures of hexagonal symmetry. Appendix B presents the effective eight-band $\mathbf{k}\cdot\mathbf{P}$ Hamiltonian that we use for describing electron states in wurtzite-type semiconductors.

II. GROWTH AND STRUCTURAL CHARACTERIZATIONS

A. Sample growth

The $In_xGa_{1-x}N$/GaN samples were grown on basal-plane oriented sapphire substrates by atmospheric pressure metal-organic chemical-vapor deposition using trimethylgallium, ammonia, disilane, and trimethylindium as precursors. After annealing the substrate at 1050 °C, a 19-nm-thick GaN nucleation layer was deposited at 525 °C. The temperature was then raised to 1080 °C, and a 2.5-μm-thick buffer layer of GaN was deposited on top of the nucleation layer. For this study five samples were prepared. In each sample a 14 periods MQW structure was grown on the GaN buffer layer at temperature of 790 °C. Each period consisted of a 2×10^{18}-cm^{-3} Si-doped 4.3-nm-thick GaN barrier layer and either a $d_w=1.2$-, 2.5-, 3.6-, 5.0-, or 6.2-nm-thick $In_{0.2}Ga_{0.8}N$ QW layer in each different sample, respectively. Following the MQW growth a 12-nm-thick $Al_{0.1}Ga_{0.9}N$ layer was deposited at low pressure. The temperature was then raised to 1060 °C, and a cap layer of a 100-nm-thick $Al_{0.1}Ga_{0.9}N$ completed the growth. In addition to these five samples, a reference sample was grown in which an 80-nm-thick layer of $In_{0.2}Ga_{0.8}N$ was deposited in place of the periodic MQW structure. The layer sequence in the sample is schematically described in the inset to Fig. 1(b). We note here that the layer thickness and their composition reported in this section are nominal as estimated from the growth parameters.[20] They vary from the actual values that were deduced from the HRXRD measurements as reported below.

B. X-ray characterization of strained hexagonal structures

The precise knowledge of atomic concentrations and strain fields is crucially important for the design and fabrication of photonic devices. In nearly perfect thin-film structures this information is hidden in the spatial distribution of lattice parameters, and it can be extracted by the aid of HRXRD. This technique provides structural characteristics with an unsurpassed precision. In the specific case of a heterostructure composed of layers containing isomorphously substituting compounds, the precision of strain determination, $\delta\varepsilon$, and that of the composition, δx, are[21]

$$\delta\varepsilon\approx\frac{\Delta d}{d},\quad \delta x\approx\frac{\Delta d}{d|\xi|},\tag{1}$$

where ξ is the lattice mismatch between the components of the heterostructure. The simple mode of data collection consists of the measurement of diffraction profiles, i.e., one-dimensional angular distributions of diffraction intensity. The structural parameters of thin films are then determined from the angular distances between the diffraction peaks originated in the films and in the substrate.[22] This procedure usually results in the determination of the relative change in lattice parameters, $\Delta d/d$, to within $(10^{-4}-5\times10^{-5})$. Better precision $(\Delta d/d\approx10^{-5})$ can be achieved by two-dimensional reciprocal-space mapping (RSM),[23,24] which utilizes about hundred diffraction profiles. More important for this study, is the fact that RSM also provides an excellent tool for determining the degree of strain relaxation in heterostructures.

These HRXRD experimental techniques are well established for layered structures with cubic symmetry. Applications of these techniques to noncubic heterostructures are in progress, dictated by the growing interest in hexagonal and rhombohedral crystals (such as GaN, SiC, Al_2O_3, and $LiNbO_3$) for microelectronics and optoelectronics. Application of HRXRD in the RSM mode to noncubic crystals is still in its infancy,[25] and a comprehensive theoretical background that is needed for its analysis is not yet developed. Therefore, we briefly present the needed background in Appendix A. For our study it was of utmost importance to establish that the control ''bulk'' $In_xGa_{1-x}N$ layer is fully strained, and that it has the same composition (x) as that of the quantum layers in the periodic structures. We used RSM measurements for this purpose.

HRXRD measurements of diffraction profiles in the vicinity of symmetric (006) GaN reflections were carried out by means of a Philips materials research diffractometer (MRD), equipped with a Cu sealed tube and a four-crystal (220) Ge monochromator. The MRD was used in the receiving slit mode of operation. A setup consisting of an 18-kW Rigaku rotating Cu anode generator combined with a Bede D^3 diffractometer was used for triple-axis scans. These scans were typically in the vicinity of the (006) and (002) GaN reflections. This setup was also used for diffraction profiles and RSM measurements in the vicinity of the asymmetric (105) GaN reflections (the inclination angle of the diffraction vector relative to the sample surface is $\varphi=20.6°$). In these cases, highly monochromatic and quasiparallel primary x-ray beams were produced using two-channel-cut (220) Si crystals. In the triple-axis mode the diffracted x rays were passed through a (220) Si channel-cut crystal analyzer, which provided high angular resolution. In order to enhance the counting rate in the RSM measurements, a 220-μm-wide receiving slit replaced the crystal analyzer in front of the x-ray detector.

Results of RSM from the reference sample and that from the $d_w=3.6$ nm MQW structure are shown in Figs. 1(a) and 1(b), respectively. In Fig. 1(a) the central condensation point ($\mathbf{H}_S$) corresponds to the maximum diffraction intensity from the GaN substrate. The condensation point from the left side ($\mathbf{H}_L$) originates from the $In_xGa_{1-x}N$ layer, which has a larger spacing between its (105) crystal planes. The condensation point ($\mathbf{H}_C$) to the right originates from the $Al_yGa_{1-y}N$ cap layer, which has smaller spacing between its planes. The slope of the straight line drawn through the points $\mathbf{H}_S$ and

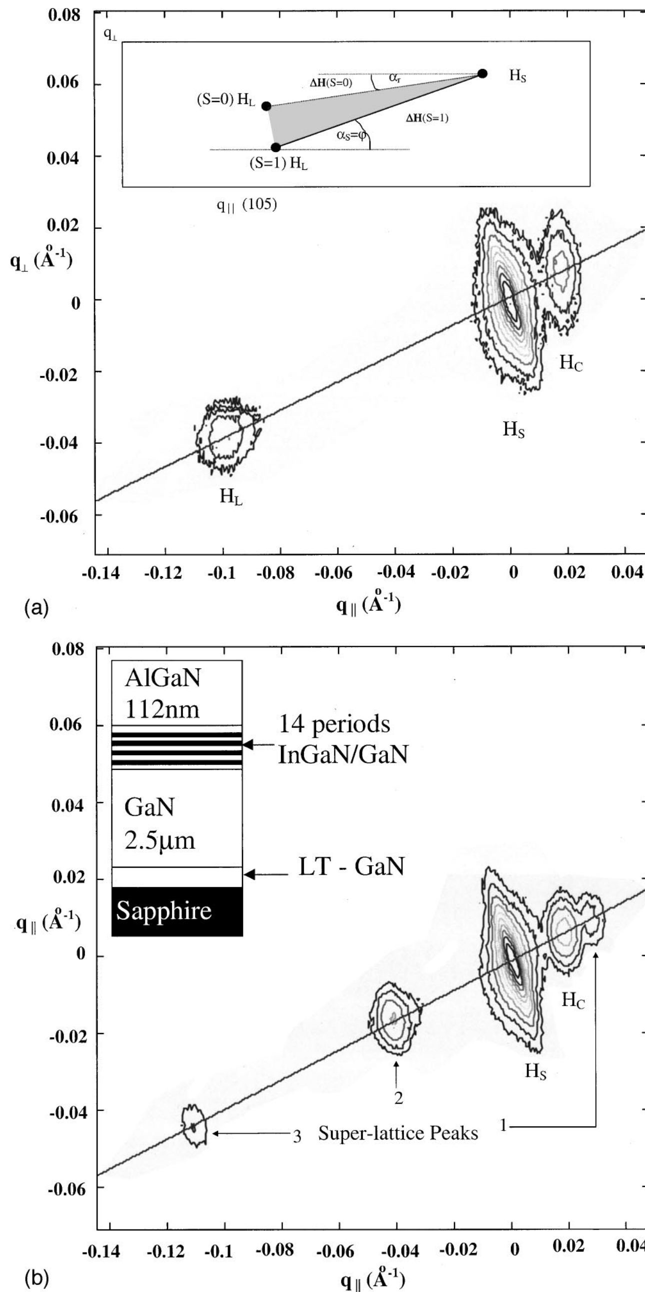

FIG. 1. Reciprocal space x-ray-diffraction mapping of the reference sample (a) and of the $d_w = 3$ nm MQW sample (b). Each contour presents a 10% variation in the diffraction intensity. The directions of the vector ΔH for the fully strained and fully relaxed cases are schematically described in the inset to (a). The layer sequence is schematically described in the inset to (b).

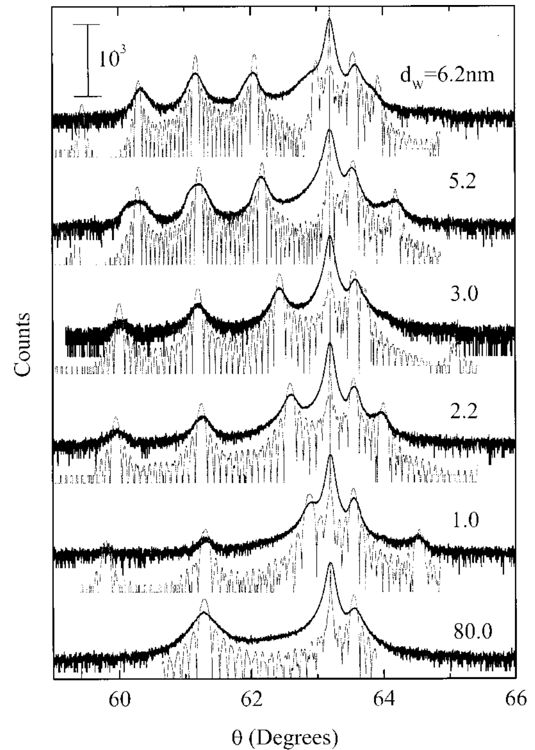

FIG. 2. Measured (bold solid line) and calculated (solid line) HRXRD profiles for the six studied In_xGaN_{1-x}/GaN structures.

$\mathbf{H}_L$, corresponds exactly to a fully strained state of the $In_xGa_{1-x}N$ film [see Eqs. (A13) and (A14)].

Once the strain state of a film is defined, its composition (x) can be straightforwardly determined from the RSM [see Eqs. (A17) and (A10)]. However, since for the RSM measurements we used a narrow slit in front of the detector, more precise data on the x values are obtained from the one-dimensional triple-axis scans, in which a crystal analyzer was used instead. The best precision is achieved when measuring symmetric reflections.[23] The data are then analyzed in terms of Eqs. (A2) and (A10) by setting $\Delta a/a$ to zero, as expected for a fully strained layer. The In content in the $In_xGa_{1-x}N$ layer was found to be $0.104 < x < 0.110$, and the Al content in the $Al_yGa_{1-y}N$ layer was found to be $0.058 < y < 0.065$. The uncertainties are due to the uncertainties in the reported values of the elastic constants of the binary nitride compounds.

The RSM from the MQW sample in Fig. 1(b) contains the central intensity condensation points $\mathbf{H}_S$ and $\mathbf{H}_C$ from the GaN substrate and cap layer, respectively. In addition, the map contains equidistantly located condensation points (1, 2, and 3) with a periodicity determined by the combined thickness, $d_w + d_b$. We note that these ''superlattice'' points are asymmetrically situated about $\mathbf{H}_S$, in accordance with the detailed analysis of Ref. 26. Here, as in the bulk sample, all the condensation points are aligned along the ''fully strained line'' ($\alpha = \varphi$). This indicates that the MQW is in a fully strained state, as well.

We proceed by assuming that the In content in all the periodic samples is exactly that of the reference sample. With this assumption, which is based on the fact that the growth parameters of all these samples were identical, we were able to simultaneously fit[27] the (006) diffraction profiles of all the studied samples. The measured and fitted profiles are shown in Fig. 2. As a result of these fittings, the MQW well and barrier thicknesses were determined to within a monolayer (without the same composition assumption the experimental error is two monolayers). The fitted values are summarized in Table I. The assumption of same In content is further validated this way, since deviations by more than $\pm 1\%$ from the accurately measured In content of the bulk sample, resulted in unacceptable fitted profiles.

TABLE I. Nominal and HRXRD measured layer thickness and composition. (The experimental uncertainties do not include the contribution from uncertainty in the bulk elastic stiffness tensor C_{ij}.)

No.	Measured AlN mole fraction	Nominal AlN mole fraction	Measured InN mole fraction	Nominal InN mole fraction	Measured d_b (nm)	Nominal D_b (nm)	Measured d_w (nm)	Nominal D_w (nm)
1	0.06 ± 0.001	0.1	0.105 ± 0.01	0.20	4.9 ± 0.3	4.3	1.0 ± 0.3	1.2
2	0.06 ± 0.001	0.1	0.105 ± 0.01	0.20	4.8 ± 0.3	4.3	2.2 ± 0.3	2.5
3	0.06 ± 0.001	0.1	0.105 ± 0.01	0.20	4.7 ± 0.3	4.3	3.0 ± 0.3	3.6
4	0.06 ± 0.001	0.1	0.105 ± 0.01	0.20	4.8 ± 0.3	4.3	5.2 ± 0.3	5.0
5	0.06 ± 0.001	0.1	0.105 ± 0.01	0.20	4.2 ± 0.3	4.3	6.2 ± 0.3	6.2
6	0.06 ± 0.001	0.1	0.105 ± 0.001	0.20				80.0

III. BAND-STRUCTURE CALCULATION

Theoretical models using multiband $\mathbf{k}\cdot\mathbf{P}$ approximations for calculating the band structure and optical properties of heterostructures of semiconductor compounds of cubic symmetry are very well established.[28] It is commonly accepted now that the simpler and much more intuitive one-band envelope-function models cannot correctly yield quantitative description of the experimental data.[28] This is mainly due to the complex nature of their valence bands, which are nonisotropic, nonparabolic, and almost degenerate. In the presence of strain and electric fields the physical picture is even more complicated, and the use of one-band models should be avoided even for a qualitative description.[28] Since these considerations hold even more strongly for wurtzite-type compounds, it is unreasonable to expect that one-band models can be used for a quantitative description of the optical properties of their heterostructures. Multiband models are therefore required for any meaningful quantitative analysis of measured data.[19]

Our model calculations proceed along the lines described by Baraff and Gershoni.[17] We use an eight-band $\mathbf{k}\cdot\mathbf{P}$ Kane-Luttinger Hamiltonian with bulk parameters for each material region. The effect of the strain is introduced to the Hamiltonian by the use of a phenomenological deformation potential theory with bulk deformation potentials. Electric fields are introduced into the Hamiltonian in a procedure described by Pistol and Gershoni.[29] The discontinuity in the material parameters and in the strain tensor elements is taken care of by a procedure discussed in Ref. 17, which is equivalent to the condition that the normal component of the probability current is continuous across internal interfaces. The method is applied to an arbitrary crystallographic direction by a simple rotation of the differential operators. We use a Fourier expansion method to convert the eight coupled differential equations into a matrix eigenvalues problem, which is then solved numerically. The method is described in detail in Refs. 17, 18, and 29 for heterostructures with bulk zincblende structure. In Appendix B we therefore present only the changes introduced to the eight-band effective Hamiltonian in order to take into account the reduced symmetry of the wurtzite-type compounds. The material parameters that we used for our calculations were compiled from the available literature. They are listed in Table II. In addition, we used Ref. 30 to relate between the strain fields and the piezoelectric fields. The symmetry properties of wurtzite-type crystals reduce the number of the independent components of their piezoelectric tensor to only three. These are commonly referred to as d_{13}, d_{33}, and d_{15}, where the index 3 corresponds to the crystallographic c axis. The heterostructures in our study were grown along this crystallographic axis. The lattice mismatch strain in this simple case gives rise to a piezoelectric field parallel to the growth direction. Its magnitude (E_3) is given by

$$E_3=\frac{2d_{13}}{\varepsilon_0\varepsilon_r}\left(C_{11}+C_{12}+\frac{2C_{13}^2}{C_{33}}\right)\varepsilon_{xx}, \tag{2}$$

where ε_0 and ε_r are the vacuum permittivity and the material static dielectric constant, respectively.

The piezoelectric constant d_{13}, which actually determines the absolute magnitude of the piezoelectric field, was used in this work as an adjustable parameter to best fit the experimental observations. The magnitude that we obtained for it is smaller than that which is reported in the literature.[31] This is possibly due to the presence of polarization fields[32] and/or due to electric field screening by charge carriers due to the modulation doping of the GaN barriers. Indeed, Si modulation doping was reported to reduce the Stokes shifts and the PL decay times.[33,34] These are strong indications for the reduction of the piezoelectric field, as we show below. Currently, our model does not take these effects into account.

In Fig. 3(a) we schematically describe a typical periodic $In_xGa_{1-x}N$/GaN quantum structure grown on the GaN buffer layer. In Fig. 3(b) the resultant potential structure for electron and hole in the lowest conduction band and highest valence band, respectively, are described. In Fig. 3(c) the calculated probability distribution of zone-center lowest-energy-state electrons and highest-energy-state holes are presented by solid and dashed lines, respectively. In Fig. 4 we present the calculated dispersion curves for the potential structure of Fig. 3(b).

IV. OPTICAL STUDIES

For the optical measurements the samples were mounted in a closed circuit helium flow optical cryostat. We used a xenon lamp's light dispersed by 0.34-m monochromator as an excitation source for the PLE measurements. For time-resolved spectroscopy the samples were excited by a frequency -doubled picosecond-pulsed radiation from a Ti:sap-

TABLE II. Material constants used in model calculations.

	$In_{0.1}Ga_{0.9}N$	InN	GaN
c (Å)	3.2265	3.544[a]	3.1892[b]
a (Å)	5.241	5.718[a]	5.185[b]
A_1	−6.56		−6.56[c]
A_2	−0.91		−0.91[c]
A_3	5.65		5.65[c]
A_4	−2.83		−2.83[c]
A_5	−3.13		−3.13[c]
A_6	−4.86		−4.86[c]
$E_{p,t}$ (eV)	15.368		15.368[c]
$E_{p,l}$ (eV)	13.056		13.056[c]
E_g (eV)	3.004[e]	1.9[d]	3.504[d]
$m_{e,l}$ (m_0)	0.191	0.115[f]	0.2[b]
$m_{e,t}$ (m_0)	0.174	0.124[f]	0.18[b]
Δ_1 (meV)	18.62	41[g]	16[b]
Δ_2 (meV)	3.61	0.33[g]	4[b]
Δ_3 (meV)	3.61	0.33[g]	4[b]
$a_{c,t}$ (eV)	−4.08		−4.08[b]
$a_{c,1}$ (eV)	−4.08		−4.08[b]
D_1	0.7		0.7[b]
D_2	2.1		2.1[b]
D_3	1.4		1.4[b]
D_4	−0.7		−0.7[b]
d_{31} (10^{-10} cm/V)	−0.765[h]	−1.1[i]	−1.7[i]
ε	10.55	15.3[i]	10.0[i]
C_{11} (10^{11} dyn/cm^2)	38.3	27.1[i]	39.6[i]
C_{12} (10^{11} dyn/cm^2)	14.2	12.4[i]	14.4[i]
C_{13} (10^{11} dyn/cm^2)	9.94	9.4[i]	10.0[i]
C_{33} (10^{11} dyn/cm^2)	37.2	20.0[i]	39.2[i]
Val. band offset (eV)	0.345[j]	1.05[i]	0

[a]Reference 45.
[b]Reference 19. Note that D_5 and D_6 are not used in this work due to the (0001) growth direction.
[c]Reference 44.
[d]Reference 3.
[e]We use a bowing parameter of 3.6 eV (Refs. 11 and 48).
[f]Reference 46.
[g]Reference 47.
[h]This work.
[i]Reference 31.
[j]Reference 49.

phire laser. The same lens, which was used for focusing the exciting beam at normal incidence on the sample surface, was also used for collecting the emitted PL. The collected light was then dispersed by a 0.22-m monochromator followed by a detector. We used either a UV-enhanced liquid-nitrogen-cooled charge-coupled device array in the cw detection mode, or a multichannel plate-cooled photomultiplier and a conventional time-correlated single-photon-counting electronics for the time-resolved spectroscopy.

A. Steady-state photoluminescence

The low-temperature PL spectra of the five MQW samples together with the PL spectrum of the reference bulk sample are presented in Fig. 5. For sample excitation, a −3.26 eV light beam was used. The excitation density was estimated to be 500 W/cm^2. This selective excitation energy, which is lower than the GaN barrier bandgap, allows us to neglect the role of carrier diffusion from the GaN layers into

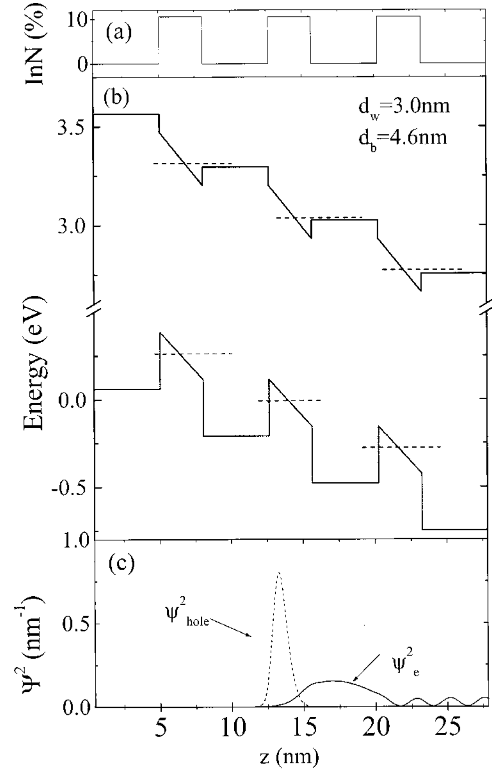

FIG. 3. Heterostructure growth sequence (a), potential structure (b), and the probability of electron (solid line) and hole (dashed line) distributions (c).

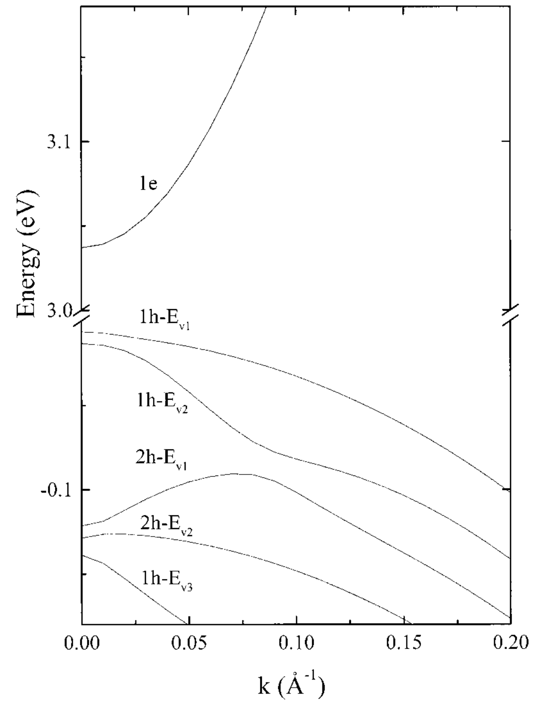

FIG. 4. Calculated electron and hole in-plane dispersion curves for the quantum structure of Fig. 3.

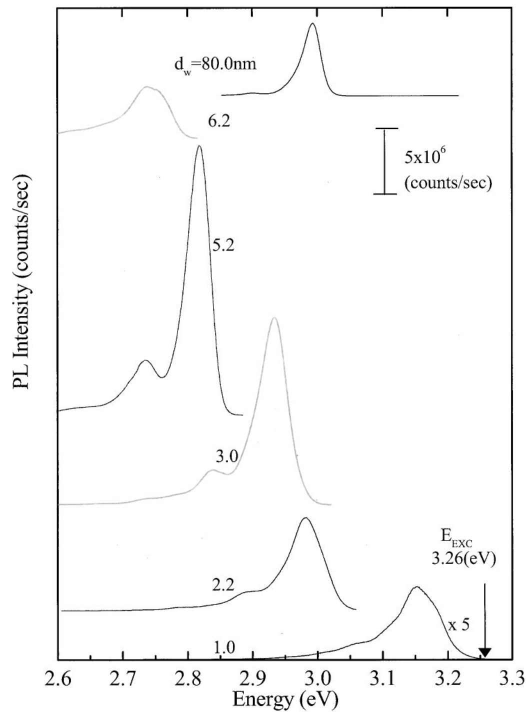

FIG. 5. cw measured low temperature PL spectra of the six studied In_xGaN_{1-x}/GaN structures.

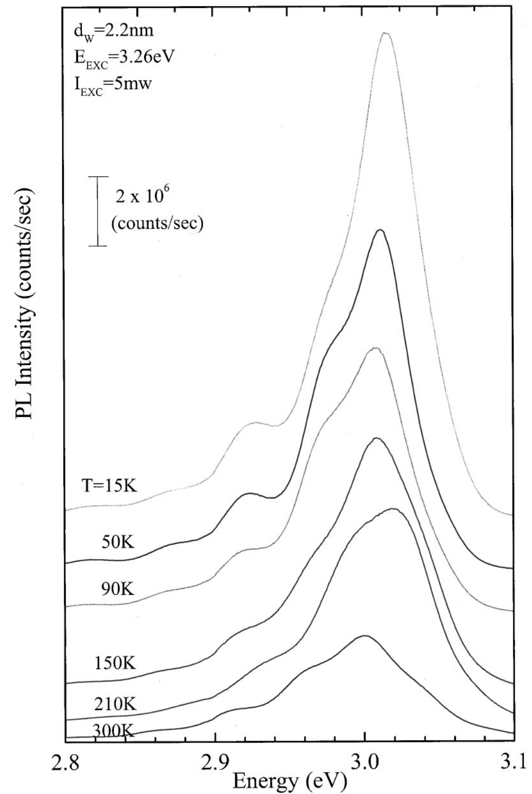

FIG. 6. PL spectra of the 2.2-nm MQW sample at various temperatures.

the MQW regions, thus simplifying the data analysis. Only the near-band-gap PL spectral lines, which are relevant for the current study, are shown in Fig. 5. In addition to the main PL lines, we observed in all the samples lower energy emission bands, which peak at 2.2 eV (not shown). These bands, which are commonly referred to as ''yellow'' bands, are due to carrier recombination at low-energy crystalline defects.[3] Their intensity was sample, temperature, and excitation density dependent, but typically few times weaker than the main spectral line shown in Fig. 5. This is indicative of the quality of the samples under study.[13]

The main spectral PL line shapes were independent of the excitation density, within more than two orders of magnitude around this excitation level. The spectrally integrated PL intensity was found to be linear with the excitation density over this dynamic range. As expected, the wider the QW's are, the lower their PL emission energy is. This dependence can only be partially accounted for by the quantum size effect.[10,13–15] A strong, strain-induced piezoelectric field, caused by the lattice mismatch between the $In_xGa_{1-x}N$ and GaN layers, significantly contributes to this dependence, as we demonstrate below. It can be seen in Fig. 5 that the PL lines are rather wide; their full spectral width at half the line maximum amount to 60–80 meV. In addition, periodic undulations in the PL intensity due to interference effects within the 2.5-μm-thick GaN buffer layers are clearly observed in all PL spectra. These broad linewidths are due to inhomogeneous broadening as a result of spatial potential variations within the optically excited area. The variations are due to composition fluctuations, strain fluctuations, interface roughness, crystal dislocations, and other defects. We noted some variations in the PL spectral shape and integrated intensity as a function of the beam position on the sample surface. This is indicative of a significant non-uniformity in the samples. The PL spectra of the 2.5-nm MQW sample for various ambient temperatures are plotted in Fig. 6. As the temperature rises, the PL line shifts slightly toward lower energies, its spectral width increases, and its integrated intensity decreases. Similar trends were also observed in all the other samples, as shown in Fig. 7, where the spectrally integrated PL intensity as a function of the samples' temperature is presented. For each sample, the intensity is normalized at the lowest measured temperature (15 K). The decrease in the PL intensity with temperature clearly indicates that the relative importance of the nonradiative recombination processes increases with the temperature. The rate, in which the PL

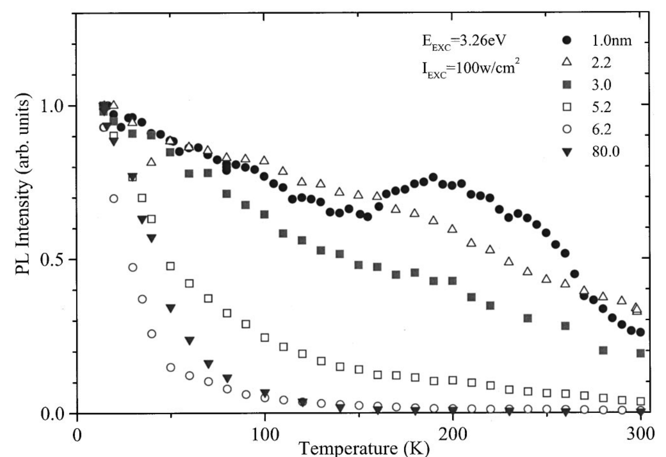

FIG. 7. Integrated PL intensity vs sample temperature for the six studied In_xGaN_{1-x}/GaN structures.

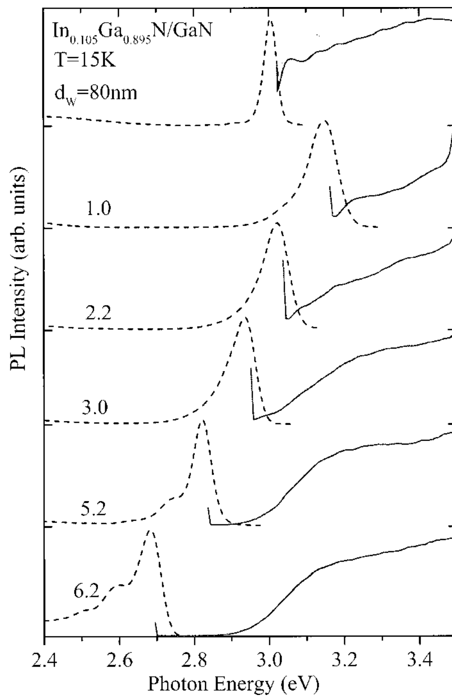

FIG. 8. PL (dashed line) and PLE (solid line) spectra of the six In_xGaN_{1-x}/GaN structures.

intensity decreases with temperature, increases with the QW width. We show quantitatively below that this is due to size dependence of the radiative lifetime and its temperature dependence, which increases with the QW width due to the presence of the piezoelectric field.

The PLE spectra of the MQW samples, together with that of the reference bulk sample, are shown in Fig. 8. For comparison in Fig. 9 we present the results of the absorption calculation based on our $\mathbf{k}\cdot\mathbf{P}$ model. In order to facilitate quantitative comparison between the measurements and calculations, the presented PLE spectra were normalized to unity at their maximum, right below the band gap of the GaN cap layer. It can be seen in Fig. 8 that the absorption edge, as determined by the PLE spectra, follows the PL peak, and it also shifts to lower energies as the QW width increases. In addition, it is seen that the energy difference between the absorption edge and the PL peak increases with the well width. The oscillator strength for optical transition, as determined from the strength of the absorption edge, significantly decreases with the QW width. These features of the measured PLE spectra are quite nicely mimicked by our model calculations. As we discuss below, they result from the presence of a large piezoelectric field ($\sim$1 MV/cm) perpendicular to the layer planes.

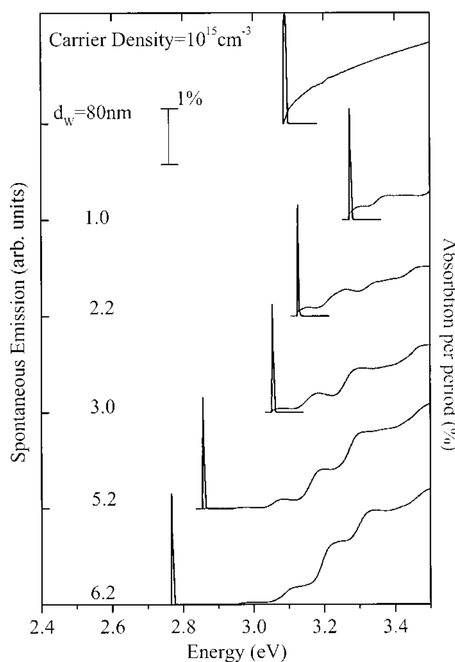

FIG. 9. Calculated emission (dashed line) and absorption (solid line) spectra of the six In_xGaN_{1-x}/GaN structures.

An excitonic resonance at the absorption edge is clearly observed in the PLE spectrum of the reference sample. Only a small exciton resonance is revealed in the PLE spectrum of the $d_w = 1.2$ nm MQW sample, and it is completely absent in the PLE spectra of MQW samples with a wider QW layer. Our model calculations do not include the excitonic effect, however, its absence from the PLE spectra of wider layer MQW samples can be readily understood in terms of the decrease in the overlap integral between the electron and hole wave functions. This is yet another consequence of the large piezoelectric field, as we discuss below. Consequently, the presence of the exciton resonance in the PLE spectrum of the bulk layer is indicative of a much smaller field there. This is probably due to a large-scale spatial redistribution of the extrinsic charges, which screens the piezoelectric field. Here we note that the maximum possible built-in field in an intrinsic, 80-nm-thick $In_{0.1}Ga_{0.9}N$ layer cannot exceed 300 kV/cm, a factor of 3 smaller than the estimated piezoelectric field in the MQW layers.

B. Time-resolved photoluminescence spectroscopy

Low-temperature, time-resolved PL spectra from one of the MQW samples are shown in Fig. 10. The spectra were measured during a time window of 200 ps at various delay times after the excitation pulse. It should be noted that the PL spectrum spectrally diffuses with time toward lower energies. This spectral diffusion is quite small in magnitude. The PL peak shifts toward lower energies by less than 7 meV, roughly 10% of the PL spectral linewidth. The lack of significant spectral diffusion indicates that transfer of excitation during the PL lifetime is absent. Quickly after their photogeneration the excitons reach their recombination sites, with no ability to reach further toward lower-energy sites. At temperatures higher than 130 K, no spectral diffusion was observed at all. We thus estimated the activation energy for excitons to leave these recombination sites as roughly 10–15 meV. These rather small localization potentials are not directly related to the much larger PL spectral linewidth, which results from the spatial inhomogeneous distribution of recombination sites within the whole area of the exciting beam. In Fig. 11 we present the peak PL transients from the 2.5-nm sample for various ambient temperatures between 15 and 300 K. Though, in general, a single exponent decay model cannot describe the transients, we have found the transients to be almost excitation density independent through the dynamic range that we investigated. This can only be

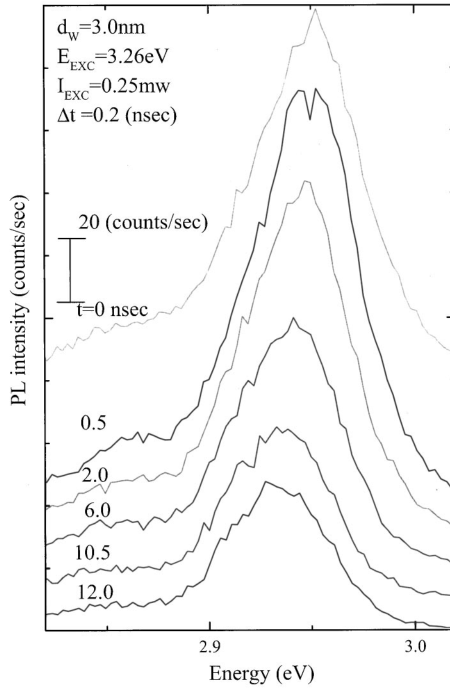

FIG. 10. Time-resolved low-temperature PL spectra of the $d_w = 3.0$ nm MQW sample.

understood in terms of different lifetimes for different localized exciton populations, which we probe while exciting at one spot.

The solid lines overlaid on the transients at their initial decay times are single-exponent decay models which best fit the data. We use these fitted curves for extracting one characteristic decay time for each measurement. By comparing single-exponent fits with two exponent fits, we safely deduced that more than 90% of the temporally integrated PL

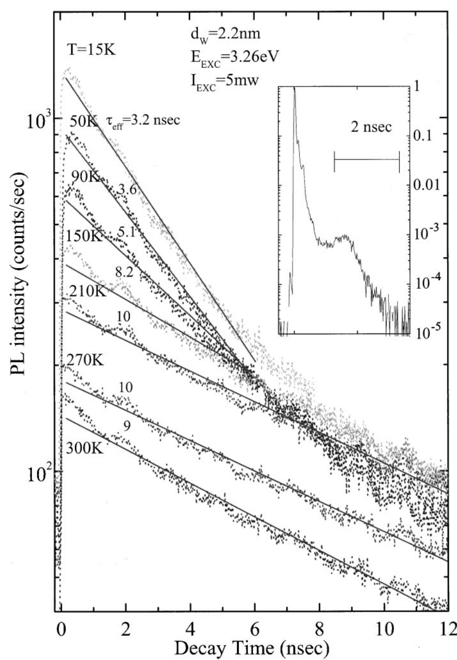

FIG. 11. The 2.2-nm sample peak PL intensity vs time after an excitation pulse for various ambient temperatures.

emission could always be described by the initial single exponent fit. An important conclusion is readily made from the decay times thus obtained: In spite of the increasing importance of the nonradiative channels as the temperature rises (see Fig. 7), the transient characteristic decay times ($\tau_{\rm eff}$) *are not* becoming shorter. The overall recombination rate ($1/\tau_{\rm eff}$) is a sum of the radiative decay rate ($1/\tau_R$) and the nonradiative one ($1/\tau_{\rm NR}$). Since the later can only increase with temperature, this means that the nonradiative rate is significantly smaller than the radiative rate. We can thus safely conclude that at low temperatures the nonradiative decay rates are slower than the radiative ones for the four narrower MQW samples.

The fitted single-exponent characteristic decay times for the MQW samples are displayed in Fig. 12 as a function of temperature. Three curves are given for each sample. Solid circles represent lifetimes deduced from the transients of the PL peaks, and solid ▲ (▼) represent lifetimes measured from transients at the lower- (higher-) energy half-maximum-intensity side of the PL peaks. Two clear trends are readily observed in Fig. 12: first, we note that the broader the QWs are the longer are their PL decay times,[13–15] second, it is clearly seen that the measured lifetimes at temperatures which are lower than 130 K are longer for lower-energy PL transients. This is more significant for MQW samples with broader QWs. While the lifetime of the PL from the 1.2-nm sample at a certain temperature varies by ±25% depending on the PL energy, these from the wider QWs vary by ±100%, significantly larger than our experimental error. Above 130 K the entire PL line has one characteristic decay time. We attributed this behavior to the typical activation energy of roughly 12 meV which is required for carriers to leave their lateral potential fluctuation traps. We note, however, that the energy range of these traps is quite large. This range determines the PL linewidth, which is typically around 60 meV. In addition, we note that the PL effective lifetime increases with temperature up to 210, 240, 250, and 50 K for the 1.2-, 2.5-, 3.6-, and 5.0-nm MQW's, respectively. At higher temperatures, the effective PL lifetime decreases with the sample temperature. For the 6.2-nm MQW and 80-nm bulk reference samples, the decay times decrease with the temperature at 15 K. By comparison with similar studies performed on $\mathrm{GaAs/Ga}_x\mathrm{Al}_{1-x}\mathrm{As}$ MQW samples,[35] we deduce that for the narrow MQW this behavior is due to thermionic emission of excitons from the QWs, which increases the nonradiative decay rate and thus effectively shortens $\tau_{\rm eff}$.[35,36] In the wider $\mathrm{In}_x\mathrm{Ga}_{1-x}\mathrm{N}$ layers another process controls the nonradiative decay rates, as discussed below.

As already mentioned, the observation that the PL lifetime increases with temperature led us to conclude that at low temperatures the nonradiative decay rates are slower than the radiative ones. Keeping this information in mind, one can safely deduce that the radiative recombination lifetime (τ_R) is inversely proportional to the PL intensity at a given excitonic density. Thus, from the temperature dependence of the measured PL intensity during a short temporal window (which is significantly shorter than the effective lifetime) around the excitation time, one can directly measure the temperature dependence of the radiative lifetime. In Fig. 13 we thus display the reciprocal of the measured PL peak intensity during a time window of 200 ps immediately after

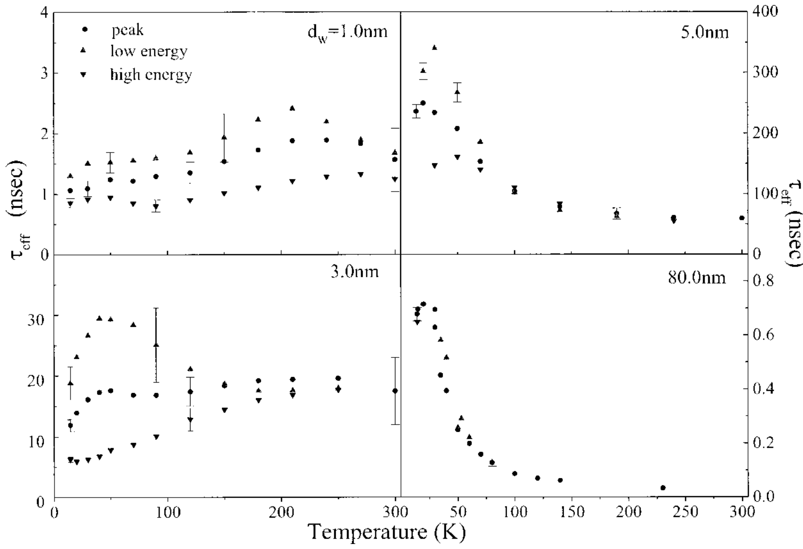

FIG. 12. Measured PL decay times vs temperatures for various emission energies. Solid ● represent lifetimes deduced from the transients of the PL peaks, and ▲ (▼) represent lifetimes measured from transients at the lower (higher) energy half-maximum intensity side of the PL spectrum. Data from four representative heterostructures are presented.

the pulse excitation, as a function of the sample temperature. In Fig. 13 we note that below 50 K, the radiative lifetime is roughly temperature independent, while between 50 to 220 K it increases linearly with the temperature.

We checked our assumptions self-consistently by calculating, for each temperature τ_R and τ_{NR}, from the measured τ_{eff} and the PL intensity shortly after the excitation. From these times the integrated PL intensity is straightforwardly calculated and compared with the measured data as given in Fig. 7.

The deduced radiative and nonradiative lifetimes as a function of temperature for the MQW samples are shown in Fig. 14. We note that both the nonradiative and radiative times are temperature dependent. While the first rapidly decreases with the temperature, the later, as already deduced from Fig. 13, increases linearly with temperature. Both times rapidly increase with the QW width. The radiative times are temperature independent at lower temperatures. This is expected for fully localized excitons.[37,38] Above 50–70 K, the radiative times increase linearly with the temperature up to about 250 K. This behavior is an unambiguous signature of the two-dimensional (2D) excitonic system. In contrast, the radiative decay times of the reference bulk sample increase faster with the temperature, as expected for a 3D system. The effective PL lifetimes of the bulk sample are much shorter than the lifetimes of the MQW samples. They also decrease more rapidly with increasing sample temperature.

We fitted the bulk measured data with an activation model similar to the one used in Ref. 36. According to this model, at low temperatures the carriers are confined within potential fluctuations, from which they recombine radiatively. The decrease in the effective lifetime and in the integrated PL intensity, as the temperature increases, is due to thermal activation of carriers out of their traps where nonradiative processes dominate the recombination. The fit, which is represented by the solid line in Fig. 14, results in an activation energy of 13 meV, a radiative lifetime of subnanosecond with temperature dependence deduced from Fig. 13, and an activated nonradiative lifetime of 20 ps.

V. DISCUSSION

The main experimental results of our studies of the optical properties of $In_xGa_{1-x}N/GaN$ MQW structures with various QW thicknesses can be summarized as follows.

(1) The PL peak positions are spectrally redshifted with

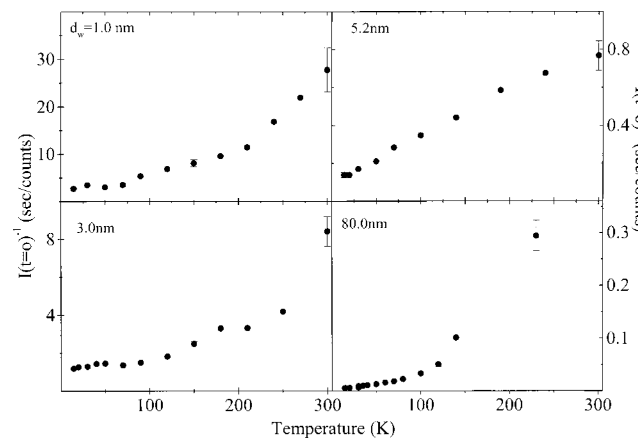

FIG. 13. The inverse of the maximum of the transient PL intensity vs sample temperature. Data from four representative heterostructures are presented.

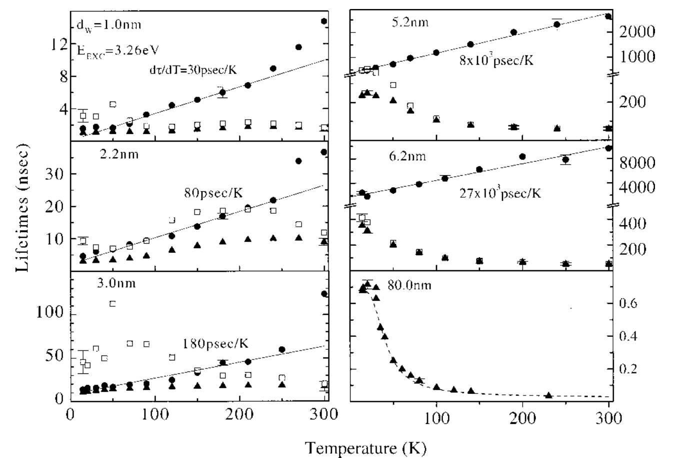

FIG. 14. The measured τ_{eff} (▲) and the deduced τ_R (●) and τ_{NR} (□) vs sample temperature. Solid lines represent the fitted linear temperature dependence of τ_R.

increasing QW width. These redshifts are much larger than anticipated by considering the quantum confinement effect in symmetric QW structures.

(2) There are large Stokes-like shifts between the band-edge PL peaks and the absorption edge as measured by PLE. These shifts increase with an increase of the QW width.

(3) Only a very small excitonic resonance occurs in the absorption edge of very narrow $In_{0.1}Ga_{0.9}N$ QWs. The excitonic resonance is not observed at all in the absorption edge of wider QWs.

(4) The spectral position of the PL peaks from MQW structures with wide QW layers ($d_w > 3$ nm) are lower in energy than that of fully strained bulk $In_{0.1}Ga_{0.9}N$ layers.

(5) The PL decay times rapidly increase with the QW width. This effect is much larger than is expected for a symmetric QW structure.

(6) The radiative lifetimes of carriers within these structures linearly increase with the sample temperature for temperatures above 50 K. This temperature dependence strongly increases with the QW width.

Two models have been recently proposed in the relevant literature in an attempt to explain the optical properties of $In_xGa_{1-x}N$/GaN quantum structures: (a) carrier localization within low-energy potential fluctuations due to the formation of indium-rich areas or islands[6–8] and (b) the presence of large piezoelectric field due to lattice mismatch strain, which leads to the quantum-confined Stark effect.[10–16] Using the experimental data presented above, we were able to set an upper limit on the magnitude of the potential fluctuations. We clearly show, by temperature-dependent time-resolved spectroscopy of MQW and bulk $In_{0.1}Ga_{0.9}N$/GaN structures, that these potential fluctuations amount to 10–15 meV only, while the PL spectral linewidth and Stokes shifts are an order of magnitude larger. We also show that the presence of the piezoelectric field largely determines the optical properties of these structures. This piezoelectric field is due to the biaxial compressive stress that the $In_xGa_{1-x}N$ layers are subjected to. The stress in these wurtzite layers induces a strong piezoelectric field along the [001] growth direction. The piezoelectric field shifts the lowest quantum-confined levels downward in energy.[9] This energy shift linearly increases with the QW width. In addition, the electric field spatially separates between the electron and hole wave functions. This separation which strongly depends on the QW width, significantly reduces the overlap integral between the electron and hole wave functions. The overlap influences the oscillator strength for optical absorption by these states. Thus the piezoelectric field determines to a large extent the optical properties of these strained MQW structures. Its presence quantitatively explains the unusual dependencies of the PL peak energy, decay time, and spectral Stokes shift on the QW width.

The measured PL energies as a function of the MQW width are presented in Fig. 15. By the dashed line we display the calculated band gap for these quantum systems, without piezoelectric field, using our eight-band $\mathbf{k}\cdot\mathbf{P}$ model and the material constants that are listed in Table II. We note that the difference between the calculated values and the measured ones linearly increases with the QW width. From this dependence, we quite accurately estimate the piezoelectric field which must be present along the growth direction of the

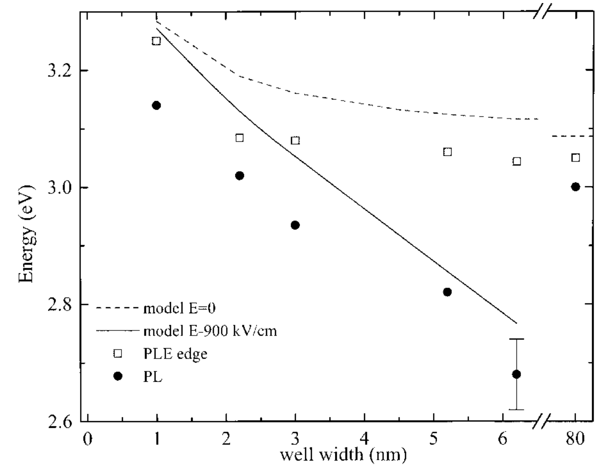

FIG. 15. PL energy (●) and PLE absorption edge (□) vs QW width. The solid (dashed) line represents the calculated band gap with (without) a piezoelectric field.

$In_{0.1}Ga_{0.9}N$ strained QWs.[10–16] Using this estimated piezoelectric field of 900 kV/cm we recalculate the MQW band gap, as shown by the solid line in Fig. 15. We note that the obtained agreement is quite good. In particular, the observation that the PL energies of the widest QWs are below the calculated bulk $In_{0.1}Ga_{0.9}N$ band gap (the dotted line in Fig. 15) is thus explained.[12,15,16]

From the temperature range in which the radiative lifetime is linearly dependent on the temperature, we extracted the proportionality constant for each QW sample. The polariton-exciton theory applied to 2D systems[39] correlates between this constant and the intrinsic radiative lifetime of an exciton with zero crystal momentum within such a system. It has been shown that this correlation is quite robust,[40] and it holds at elevated temperatures even for systems where quite large localizing potentials exist. In these cases this correlation is given by

$$\frac{\partial \tau_R}{\partial T} = \frac{2 M_X k_B}{\hbar^2 k_0^2}\,\tau_0, \tag{3}$$

where M_X is the 2D exciton effective mass, k_0 is the wave vector of the photon at the excitonic resonance, and τ_0 is the intrinsic radiative lifetime of the 2D system.[39,41] In Fig. 16 we present the intrinsic radiative lifetimes that we deduced from our measurements as a function of the QW width. We note that these times depend very strongly on the QW width. In fact, only such a weak dependence is expected in systems where these widths are comparable to the bulk exciton radius, since τ_0 is proportional to the reciprocal of the excitonic oscillator strength for optical transition.[39–41] Indeed, in $Ga_xAl_{1-x}As$/GaAs MQWs with $4 < d_w < 18$ nm, where the bulk exciton radius is 10 nm, an increase in the intrinsic radiative lifetime of roughly a factor of 2 is predicted[39] and measured.[38] In Fig. 16 we show that in the $In_xGa_{1-x}N$/GaN system, where the bulk exciton radius is estimated to be 3.4 nm, the increase in the intrinsic lifetimes with increasing QW width is orders of magnitude larger. Here the built in piezoelectric field, which separates the electron-hole pair, dramatically reduces their overlap integral. Consequently,

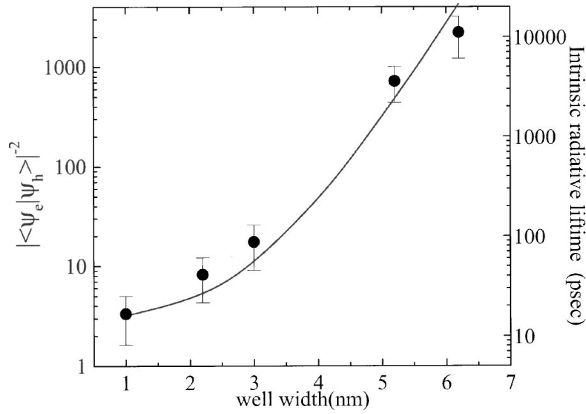

FIG. 16. Intrinsic radiative lifetimes vs QW width. The solid line represents the reciprocal of the calculated electron-hole wave-function overlap integral.

the oscillator strength for their optical recombination decreases, and their radiative lifetimes increase.

We estimate this effect by utilizing our $\mathbf{k}\cdot\mathbf{P}$ program (see Appendix B) to calculate the oscillator strength for optical transitions across the band gap in the presence of a 900-kV/cm piezoelectric field.[27,30] The solid line in Fig. 16 represents the reciprocal of the calculated oscillator strength, vs the QW width d_w. A relatively good agreement is obtained with the experimentally determined dependence of the intrinsic radiative lifetimes on the QW width.

VI. SUMMARY

We used optical spectroscopy and high-resolution x-ray diffraction in order to characterize and study a set of $In_xGa_{1-x}N/GaN$ quantum structures. The application of these rather conventional characterization tools to this technologically important material system of hexagonal symmetry are theoretically outlined and used for careful analysis of our experimental observations. We show that the absorption and emission spectra of these structures and their temporal and temperature dependencies are fundamentally different from these of comparable structures with cubic symmetry. We clearly demonstrate that these differences are due to the presence of a strong strain-induced piezoelectric field along a sixfold symmetry axis. The strain levels in the studied structures are precisely measured by x-ray mapping in reciprocal space. The magnitude of this piezoelectric field is quite accurately estimated from a theoretical analysis of the measured *cw* and time-resolved optical spectra.

We observed that the energy difference between the absorption edge and the PL peak drastically increases with the QW width. The PL decay time drastically increases with the QW width[13–15] and with its temperature as well. We quite accurately determined the radiative and nonradiative decay times of excitons in these structures from the measured decay times, the integrated PL intensity, and the PL intensity immediately after the excitation pulse. The intrinsic radiative lifetimes, which are inversely proportional to the exciton oscillator strengths, are then calculated from the temperature dependence of the determined radiative lifetimes. We find that the QW width dependence of the intrinsic radiative lifetime is much stronger, in these III-nitride compounds, than that of other III-V systems of narrower band gaps.[37,38]

Our experimental findings were analyzed using an eight-band $\mathbf{k}\cdot\mathbf{P}$ model[17,18] that we modified in order to take into account the hexagonal symmetry of this system.[19] Our model quantitatively explains both the Stokes shifts and the intrinsic radiative lifetimes that we measured. Their strong dependencies on the QW width are also explained in terms of a large strain-induced piezoelectric field along the growth direction.

ACKNOWLEDGMENTS

This work was supported by the P. and E. Nathan Research Fund at the Technion, and by the Israel Science Foundation founded by the Israel Academy of Sciences and Humanities under Contract No. 335/99, and by the Technion Research Fund. Wolfson Center for Interface Studies at the Technion is gratefully acknowledged for free access to the x-ray-diffraction facility.

APPENDIX A: ANALYSIS OF X-RAY RECIPROCAL SPACE MAPS FROM HETEROSTRUCTURES OF HEXAGONAL SYMMETRY COMPOUNDS

We denote the hexagonal lattice parameters of the substrate (film) by $a(a+\Delta a)$ and $c(c+\Delta c)$, respectively. The difference $\Delta\Theta_B$ between the Bragg angles for (*hkl*) atomic planes in the substrate (and film)—$\Theta_B(\Theta_B+\Delta\Theta_B,)$—can be easily calculated by differentiating the Bragg equation $2d\sin\Theta_B=\lambda$, where

$$d^{-1}=\sqrt{\left(\frac{4}{3}\frac{h^2+hk+k^2}{a^2}+\frac{l^2}{c^2}\right)^{1/2}}, \tag{A1}$$

and λ represents the x-ray wavelength. Thus

$$\Delta\Theta_B=-\tan\Theta_B\left(\frac{\Delta a}{a}\sin^2\varphi+\frac{\Delta c}{c}\cos^2\varphi\right). \tag{A2}$$

$\Delta a/a \ll 1$ and $\Delta c/c \ll 1$, where φ is the angle between the appropriate vector of the reciprocal lattice $\mathbf{H}=(hkl)$ $\times(|\mathbf{H}|=2\pi/d)$ and the vector (001), which in our case is along the growth direction. We obtain

$$\cos\varphi=\frac{l/c}{\sqrt{\left(\frac{4}{3}\frac{(h^2+hk+k^2)}{a^2}+\frac{l^2}{c^2}\right)^{1/2}}}. \tag{A3}$$

For basal plane-oriented layers, the vector (001) coincides with the normal to the sample surface. In general, due to differences between lattice parameters, the atomic planes (*hkl*) of the substrate and those of the film are not parallel, but intersect at a certain angle, which we denote by $\Delta\omega$:

$$\Delta\omega=\frac{\sin 2\varphi}{2}\left|\frac{\Delta a}{a}-\frac{\Delta c}{c}\right|. \tag{A4}$$

Diffraction profile measurements in the vicinity of asymmetric reflections ($\varphi\neq 0$ and $\varphi\neq 90°$) provide information on both $\Delta\Theta_B$ and $\Delta\omega$. This, in turn, allows us to determine both $\Delta a/a$ and $\Delta c/c$.

Elasticity considerations impose certain constraints on possible modifications of lattice constants of epitaxially

grown films. It is well known that the normal to the surface stress component, σ_{33} (3 denotes the c axis, i.e., the growth direction in our case) strictly vanishes. Therefore, for basal plane oriented layers one obtains

$$\sigma_{33}=C_{13}(\varepsilon_{11}+\varepsilon_{22})+C_{33}\varepsilon_{33}=0 \tag{A5}$$

where C_{ij} are the components of the elastic stiffness tensor. Due to the symmetry in the basal plane, $\varepsilon_{11}=\varepsilon_{22}$, and thus

$$\varepsilon_{33}=-K\varepsilon_{11}, \tag{A6}$$

where

$$K=2\frac{C_{13}}{C_{33}}. \tag{A7}$$

Assuming that isomorphously substituted compounds are characterized by their lattice constant mismatches ξ_a and ξ_c, respectively, the strain tensor components $\varepsilon_{11}=\varepsilon_{22}$ in the hexagon plane are then given by

$$\varepsilon_{11}=-Sx\xi_a. \tag{A8}$$

In Eq. (A8), x, is the content of the substituting compound and $0\leqslant S\leqslant 1$ is the strain degree, which depends on the density of misfit dislocations at the film/substrate interface. A fully strained film with hexagons that completely match those of the substrate corresponds to $S=1$. A fully relaxed film with hexagons sides that are independent from those of the substrate corresponds to $S=0$.

Using Eqs. (A6) and (A8), the modifications of the film lattice parameters a and c, relative to the corresponding substrate parameters, can be written in the following forms:

$$\frac{\Delta a}{a}=(1-S)x\xi_a, \tag{A9}$$

$$\frac{\Delta c}{c}=x(\xi_c+KS\xi_a). \tag{A10}$$

Equations (A9) and (A10) can be used for determination of the x and S values via the measured strain-induced changes in the lattice constants $\Delta a/a$ and $\Delta c/c$. Unfortunately, in many cases the precision of the obtained data is not high enough due to the overlap between the diffraction peaks from the film and those from the substrate. This overlap is more pronounced when asymmetric reflections are used.[23] The RSM measurements do not suffer from this drawback, and they ensure better precision in the measured data since they provide a two-dimensional distribution of the diffraction intensity in the scattering plane. Experimentally, the intensity scans are performed in the vicinity of the appropriate node **H** of the reciprocal lattice along two orthogonal directions: parallel to the vector **H** (the $\mathbf{q}\|$ axis, which connects the origin with the **H** node in the reciprocal lattice), and perpendicular to **H** (the $\mathbf{q}\perp$ axis).

Below, we illustrate the advantages of the RSM technique for the determination of the strain degree, $0\leqslant S\leqslant 1$. Due to the differences between the lattice constants of the substrate and film, there is also a difference, $\Delta\mathbf{H}=\mathbf{H}_L-\mathbf{H}_S$, between the reciprocal vector of the layer, $\mathbf{H}_L$ and that of the substrate, $\mathbf{H}_S$. The projections of the difference vector $\Delta\mathbf{H}$ on the $\mathbf{q}_\|$ and $\mathbf{q}_\perp$ axes are given by

$$\Delta\mathbf{H}_{\mathbf{q}\|}=|\Delta\mathbf{H}|\Delta\Theta_B\tan^{-1}(\Theta_B),$$

$$\Delta\mathbf{H}_{\mathbf{q}\perp}=|\Delta\mathbf{H}|\Delta\omega, \tag{A11}$$

where $\Delta\Theta_B$ and $\Delta\omega$ are given by Eqs. (A2) and (A4), respectively. Thus the line connecting $\mathbf{H}_L$ and $\mathbf{H}_S$ is inclined to the $\mathbf{q}_\|$ axis with an inclination angle α, which satisfies

$$\tan\alpha=\frac{\Delta\mathbf{H}_{\mathbf{q}\perp}}{\Delta\mathbf{H}_{\mathbf{q}\|}}=\frac{\left|\frac{\Delta a}{a}-\frac{\Delta c}{c}\right|\frac{\sin 2\varphi}{2}}{\frac{\Delta a}{a}\sin^2\varphi+\frac{\Delta c}{c}\cos^2\varphi}. \tag{A12}$$

Using Eqs. (A9) and (A10), we obtain

$$\tan\alpha=\frac{\xi_c-\xi_a(1-S)+\xi_aKS}{\xi_c+\xi_a(1-S)\tan^2\varphi+\xi_aKS}\tan\varphi. \tag{A13}$$

Equation (A13) provides a precise method for determining S simply by drawing a straight line (the $\Delta\mathbf{H}$ vector) on the two-dimensional x-ray map along which the intensity distribution is concentrated. The slope of this line is $\tan\alpha$, and it determines S according to Eq. (A13). It is important to note that Eq. (A13) does not contain x, and therefore the determination of the strain state S is composition independent. The possible slopes of the vector $\Delta\mathbf{H}$ [see the inset in Fig. 1(a)] are bound between that for a fully strained state $(S=1)$ and that for a fully relaxed state $(S=0)$. Using Eq. (A13), we find that the fully strained case corresponds to

$$\tan\alpha_S=\tan\varphi,$$

$$\alpha_S=\varphi. \tag{A14}$$

The same slope is obtained for a heterostructure composed of layers of cubic symmetry.[23] This reflects the fact that in a fully strained heterostructure the vector $\Delta\mathbf{H}$ is parallel to the growth direction independently of the unit-cell symmetry. Its projections parallel and perpendicular to the vector **H** are $\Delta\mathbf{H}_{\mathbf{q}\|}=|\Delta\mathbf{H}|\cos\varphi$ and $\Delta\mathbf{H}_{\mathbf{q}\perp}=|\Delta\mathbf{H}|\sin\varphi$, respectively. Note that slope (A14) does not depend on K, and therefore does not depend on the elastic stiffness constants, which are often not accurately known.

The slope for the fully relaxed state is given by

$$\tan\alpha_r=\frac{\xi_c-\xi_a}{\xi_c+\xi_a\tan^2\varphi}\tan\varphi. \tag{A15}$$

Note that for hexagonal symmetry $a_r\neq 0$, i.e., differs from the known result for cubic heterostructures, where a_r strictly vanishes[24] [this can be easily verified by substituting $x_a=x_c$ in Eq. (A15)]. For the (105) asymmetric reflection, which we used in the RSM measurements of the $In_xGa_{1-x}N$/GaN heterostructures, a value of $a_r=2°$ is calculated. The RSM also contains information about the In content. In fact, the projection of the vector $\Delta\mathbf{H}=\mathbf{H}_S-\mathbf{H}_L$ on the horizontal axis ($\mathbf{q}_\|$) determines the modification of the d spacing:

$$\frac{\Delta d}{d}=\frac{\Delta\mathbf{H}_{\mathbf{q}\|}}{|\Delta\mathbf{H}|}=\frac{\Delta a}{a}\sin^2\varphi+\frac{\Delta c}{c}\cos^2\varphi \tag{A16}$$

[see Eq. (A2)]. In the case of a fully strained heterostructure ($\Delta a = 0$), Eq. (A16) transforms into

$$\frac{\Delta d}{d} = \frac{\Delta c}{c}\cos^2\varphi. \tag{A17}$$

Equation (A17) with Eq. (A10) can be used for a determination of the composition (x) of the thin films.

APPENDIX B: EIGHT-BAND EFFECTIVE HAMILTONIAN FOR STRAINED BULK CRYSTALS WITH WURTZITE SYMMETRY

The rows and columns of the effective Hamiltonian are labeled by zone-center Bloch waves in the order[17] $|s\uparrow\rangle$, $|x\uparrow\rangle$, $|y\uparrow\rangle$, and $|z\uparrow\rangle$ followed by their time reversal conjugates $|s\downarrow\rangle$, $|x\downarrow\rangle$, $|y\downarrow\rangle$, and $|z\downarrow\rangle$, respectively. Where the z axis is chosen to be the wurtzite crystal c axis. In this basis the effective Hamiltonian matrix $\mathbf{H}$ takes the form

$$\mathbf{H} = \begin{bmatrix} G(k) & \Gamma \\ -\Gamma^* & G^*(k) \end{bmatrix}. \tag{B1}$$

We follow Kane[42] in defining the matrices $G(\mathbf{k})$ and Γ: $G(\mathbf{k}) = G_1(\mathbf{k}) + G_2(\mathbf{k}) + G_{SO} + G_{\text{strain}}(\mathbf{k})$, where $\mathbf{k}$ is the electron crystal momentum, and the matrices that define the effective Hamiltonian are given by:

$$G_1 \equiv \begin{bmatrix} E_c & ik_xP_t & ik_yP_t & ik_zP_l \\ -ik_xP_t & E_v+\Delta_l & 0 & 0 \\ -ik_yP_t & 0 & E_v+\Delta_l & 0 \\ -ik_zP_l & 0 & 0 & E_v \end{bmatrix}, \tag{B2}$$

$$G_2 \equiv \begin{bmatrix} A_1(k_x^2+k_y^2)+A_1k_z^2 & B_1k_yk_z & B_1k_xk_z & B_2k_xk_y \\ B_1k_yk_z & L_1'k_x^2+M_1(k_y^2+k_z^2) & N_1'k_xk_y & N_2'k_xk_z \\ B_1k_xk_z & N_1'k_xk_y & M_1k_x^2+L_1'k_y^2+M_2k_z^2 & N_2'k_xk_z \\ B_2k_xk_y & N_2'k_xk_z & N_2'k_xk_z & M_3k_x^2+M_3k_y^2+L_2'k_z^2 \end{bmatrix}, \tag{B3}$$

$$G_{\text{so}} \equiv -\Delta_2 \begin{bmatrix} 0 & 0 & 0 & 0 \\ 0 & 0 & i & 0 \\ 0 & -i & 0 & 0 \\ 0 & 0 & 0 & 0 \end{bmatrix}, \tag{B4}$$

$$\Gamma \equiv -\Delta_3 \begin{bmatrix} 0 & 0 & 0 & 0 \\ 0 & 0 & 0 & -1 \\ 0 & 0 & 0 & i \\ 0 & 1 & -i & 0 \end{bmatrix}. \tag{B5}$$

The Bloch matrix elements P_t, P_l, E_c, E_v, Δ_1, Δ_2, and Δ_3 are defined as

$$P_t = -i\frac{\hbar}{m_0}\langle s\uparrow|p_x|x\uparrow\rangle = -i\frac{\hbar}{m_0}\langle s\uparrow|p_y|x\uparrow\rangle, \tag{B6}$$

$$P_1 = -i\frac{\hbar}{m_0}\langle s\uparrow|p_z|z\uparrow\rangle,$$

$$E_c = \left\langle s\uparrow\left|\frac{p^2}{2m_0}+V(r)\right|s\uparrow\right\rangle,$$

$$E_v = \left\langle z\uparrow\left|\frac{p^2}{2m_0}+V(r)\right|z\uparrow\right\rangle,$$

$$E_v+\Delta_1 \equiv \left\langle x\uparrow\left|\frac{p^2}{2m_0}+V(r)\right|x\uparrow\right\rangle = \left\langle y\uparrow\left|\frac{p^2}{2m_0}+V(r)\right|y\uparrow\right\rangle,$$

$$\Delta_2 = \frac{i\hbar}{4m_0^2c^2}\langle x|(\nabla V\times p)_z|y\rangle,$$

$$\Delta_3 = \frac{i\hbar}{4m_0^2c^2}\langle y|(\nabla V\times p)_x|z\rangle = \frac{i\hbar}{4m_0^2c^2}\langle z|(\nabla V\times p)_y|x\rangle.$$

Here $\hbar$, m_0, and c are the reduced Planck's constant, the electron rest mass, and the speed of light, respectively, $\mathbf{p}$ is the electron momentum operator, and $V(r)$ is the crystallographic potential that the electron is subjected to. The Bloch matrix elements in Eq. (B6) are regarded as bulk material constants and they are usually found by comparison with experimental data or theoretical band-structure calculations. The constants that we used in our calculations are listed in Table II, where $P_t(P_l)$ is given in terms of the conduction to valence-band optical matrix elements $E_{\mathbf{p}\,t(l)}$:

$$P_{t(l)}^2 = (\hbar^2/2m_0)E_{\mathbf{p}\,t(l)}.$$

The eight-band coupling constants: L_1', L_2', M_1', M_2', M_3', N_1', N_2', B_1, and B_2 in Eq. (B2) are defined in Ref. 19. They are related to Pikus and Bir's six-Band parameters A_1-A_6,[43]

$$L_1'=\frac{\hbar^2}{2m_0}(A_2+A_4+A_5)+\frac{P_t^2}{E_g},$$

$$L_2'=\frac{\hbar^2}{2m_0}A_1+\frac{P_l^2}{E_g},$$

$$N_1'=\frac{\hbar^2}{2m_0}2A_5+\frac{P_t^2}{E_g},$$

$$N_2'=\frac{\hbar^2}{2m_0}A_6\sqrt{2}+\frac{P_tP_l}{E_g}, \tag{B7}$$

$$M_1'=\frac{\hbar^2}{2m_0}(A_2+A_4-A_5),$$

$$M_2'=\frac{\hbar^2}{2m_0}(A_1+A_3),$$

$$M_3'=\frac{\hbar^2}{2m_0}A_2,$$

where we use the hexagonal symmetry relation $L_1'-M_1'=N_1'$.[19]

The terms B_1 and B_2, which strictly vanish for crystals of diamond symmetry, are set in this work to zero. The diagonal conduction band term $A_t(A_l)$ is related to the transversal (longitudinal) electron effective mass $m_{e,t}(m_{e,l})$:

$$A_t=\frac{\hbar^2}{2m_0}\left(\frac{m_0}{m_{e,t}}\right)-P_t^2\frac{E_g-\Delta_1+\Delta_2}{[E_g(E_g-\Delta_1+\Delta_2)-2\Delta_3^2]},$$
$$A_1=\frac{\hbar^2}{2m_0}\left(\frac{m_0}{m_{e,l}}\right)-P_1^2 \times\frac{E_g(E_g-\Delta_1)-\Delta_3^2}{[E_g(E_g-\Delta_1+\Delta_2)-2\Delta_3^2](E_g-\Delta_1-\Delta_2)}. \tag{B8}$$

Here $E_g=E_C-E_v$ is the "bare" fundamental energy band gap. Note that the actual bandgap is given by $E_g-\max(E_{vj})$, where Ev_j, $j=1$, 2, and 3 are the valence-band zone-center energies:

$$E_{v1}=E_v+\Delta_1+\Delta_2,$$

$$E_{v2}=E_v+\frac{\Delta_1-\Delta_2}{2}+\sqrt{\left[\left(\frac{\Delta_1-\Delta_2}{2}\right)^2+2\Delta_3^2\right]^{1/2}}, \tag{B9}$$

$$E_{v3}=E_v+\frac{\Delta_1-\Delta_2}{2}-\sqrt{\left[\left(\frac{\Delta_1-\Delta_2}{2}\right)^2+2\Delta_3^2\right]^{1/2}}.$$

We note here that A_t and A_l are relatively small in these wide-band-gap materials, and that they were neglected in Ref. 19. The strain interaction couples parallel spin terms only, and from symmetry considerations G_{strain} has a similar form to G_2:

$$G_{\mathrm{Strain}}=\begin{pmatrix} a_{Ct}(\varepsilon_{xx}+\varepsilon_{yy})+a_{Cl}\varepsilon_{zz} & b_1'\varepsilon_{yz}-i\sum\limits_{j=x,y,z}(P_j\varepsilon_{xj}k_j) & b_t'\varepsilon_{xz}-i\sum\limits_{j=x,y,z}(P_j\varepsilon_{yj}k_j) & b_1'\varepsilon_{xy}-i\sum\limits_{j=x,y,z}(P_j\varepsilon_{zj}k_j) \\ b_1'\varepsilon_{yz}+i\sum\limits_{j=x,y,z}(P_j\varepsilon_{xj}k_j) & 1_1\varepsilon_{xx}+m_1\varepsilon_{yy}+m_2\varepsilon_{zz} & n_1\varepsilon_{xy} & n_2\varepsilon_{xz} \\ b_t'\varepsilon_{xz}+i\sum\limits_{j=x,y,z,}(P_j\varepsilon_{yj}k_j) & n_1\varepsilon_{xy} & m_1\varepsilon_{xx}+l_1\varepsilon_{yy}+m_2\varepsilon_{zz} & n_2\varepsilon_{yz} \\ b_1'\varepsilon_{xy}+i\sum\limits_{j=x,y,z}(P_j\varepsilon_{zj}k_j) & n_2\varepsilon_{xz} & n_2\varepsilon_{yz} & m_3\varepsilon_{xx}+m_3\varepsilon_{yy}+l_2\varepsilon_{zz} \end{pmatrix}, \tag{B10}$$

where $P_{1,2}=P_t$, $P_3=P_1$, and $a_{Ct(Cl)}$, is the conduction band transverse (longitudinal) deformation potential.

The relations between the strain coupling-constants l_1, l_2, m_1, m_2, m_3, n_1, and n_2 to Pikus and Bir's six-band strain deformation potentials D_1-D_6,[43] are similar in form to the relations of Eqs. (B7):

$$l_1=D_2+D_4+D_5, \tag{B11}$$

$$l_2=D_1,$$

$$n_1=2D_5,$$

$$n_2=\sqrt{2}D_6,$$

$$m_1=D_2+D_4-D_5,$$

$$m_2=D_1+D_3,$$

$$m_3=D_2.$$

In an analogous way, b_t' and b_1' are also set to zero in this work. The deformation potentials that we used are listed in Table II.

[1] S. Nakamura and G. Fasol, *The Blue Laser Diode* (Springer, Berlin, 1997).
[2] I. Akasaki and H. Amano, Jpn. J. Appl. Phys., Part 1 **36**, 5393 (1997).
[3] *Group III Nitride Semiconductor Compounds, Physics and Applications*, edited by B. Gil (Clarendon Press, Oxford, 1998).
[4] S. Nakamura, IEEE J. Sel. Top. Quantum Electron. **4**, 483 (1998).
[5] M. D. McCluskey, L. T. Romano, B. S. Krusor, D. P. Bour, N. M. Johnson, and S. Brennan, Appl. Phys. Lett. **72**, 1730 (1998).
[6] Y. Narukawa, Y. Kawakami, S. Fujita, and S. Nakamura, Phys. Rev. B **55**, R1938 (1997).
[7] S. Chichibu, T. Sota, K. Wada, and S. Nakamura, J. Vac. Sci. Technol. B **16** (4), 2204 (1998).
[8] K. P. O'Donnell, R. W. Martin, and P. G. Middleton, Phys. Rev. Lett. **82**, 237 (1999).
[9] D. A. B. Miller, D. S. Chemla, T. C. Damen, A. C. Gossard, W. Wiegmann, T. H. Wood, and C. A. Burrus, Phys. Rev. Lett. **53**, 2173 (1984).
[10] T. Takeuchi, S. Sota, M. Katsuragawa, M. Komori, H. Takeuchi, H. Amano, and I. Akasaki, Jpn. J. Appl. Phys., Part 1 **36**, L382 (1997).
[11] C. Wetzel, T. Takeuchi, H. Amano, and I. Akasaki, J. Appl. Phys. **85**, 3786 (1999).
[12] S. F. Chichibu, A. C. Abare, M. S. Minsky, S. Keller, S. B. Fleicher, J. E. Bowers, E. Hu, U. K. Mishra, L. A. Coldern, and S. P. DenBaars, Appl. Phys. Lett. **73**, 2005 (1998).
[13] J. S. Im, H. Kollmer, J. Off, A. Sohmer, F. Scholz, and A. Hangleiter, Phys. Rev. B **57**, R9436 (1998).
[14] A. Hangleiter, J. S. Im, H. Kollmer, S. Heppel, J. Off, and F. Scholz, MRS Internet J. Nitride Semicond. Res. **3**, 15 (1998).
[15] E. Berkowicz, D. Gershoni, G. Bahir, A. C. Abare, S. P. Denbaars, and L. C. Coldern, in *Physics of Semiconductors*, edited by D. Gershoni (World Scientific, Singapore, 1999), p. 251.
[16] B. Gil, P. Lefebvre, J. Allegre, H. Mathieu, N. Grandjean, M. Leroux, J. Massies, P. Bigenwald, and P. Christol, Phys. Rev. B **59**, 10 246 (1999), and references therein.
[17] G. A. Baraff and D. Gershoni, Phys. Rev. B **43**, 4011 (1991).
[18] D. Gershoni, C. H. Henry, and G. A. Baraff, IEEE J. Quantum Electron. **29**, 2433 (1993).
[19] S. L. Chuang and C. S. Chang, Phys. Rev. B **54**, 2491 (1996); Semicond. Sci. Technol. **12**, 252 (1997).
[20] A. C. Abare, S. Keller, M. P. Mack, L. A. Coldern, and S. P. DenBaars, *1997 Digest of the IEEE/LEOS Summer Topical Meetings*, Cat. No. 97TH8276 (IEEE, New York, 1997), pp. 25–26.
[21] E. Zolotoyabko, A. Goldner, and Y. Komem, Phys. Rev. B **60**, 11 014 (1999).
[22] W. J. Bartels, J. Honstra, and D. J. Lobeek, Acta Crystallogr., Sect. A: Found. Crystallogr. **42**, 539 (1986).
[23] D. K. Bowen and B. K. Tanner, *High Resolution X-Ray Diffractiometry and Topography* (Taylor & Francis, London, 1998).
[24] V. Holy, U. Pietcsh, and T. Baumbach, *High-Resolution X-Ray Scattering from Thin Films and Multilayers* (Springer-Verlag, Berlin, 1999).
[25] M. Leroux, N. Grandjean, M. Laugt, J. Massies, B. Gil, P. Lefebvre, and P. Bigenwald, Phys. Rev. B **58**, R13 371 (1998).
[26] I. Goldfarb, E. Zolotoyabko, and D. Shechtman, J. Appl. Phys. **74**, 2501 (1992).
[27] P. Fewster, Semicond. Sci. Technol. **8**, 1915 (1993).
[28] G. Bastard, in *Wave Mechanics Applied to Semiconductor Heterostructures* (Wiley, New York, 1988), pp. 41–51.
[29] M.-E. Pistol and D. Gershoni, Phys. Rev. B **50**, 11 738 (1994).
[30] A. Bykhovski, B. Gelmont, and M. Shur, J. Appl. Phys. **74**, 6734 (1993).
[31] G. Martin, A. Botchkarev, A. Rockett, and H. Morkoc, Appl. Phys. Lett. **68**, 2541 (1996).
[32] F. Bernardini, V. Fiorentini, and D. Vanderbilt, Phys. Rev. B **56**, R10 024 (1997).
[33] Y. Cho, J. J. Song, S. Keller, M. S. Minsky, E. Hu, U. K. Mishra, and S. P. DenBaars, Appl. Phys. Lett. **73**, 1128 (1998).
[34] S. Chichibu, D. A. Cohen, M. P. Mack, A. C. Abare, P. Kozodoy, M. Minsky, S. Fleischer, S. Keller, J. E. Bowers, U. K. Mishra, L. A. Coldern, D. R. Clarke, and S. P. DenBaars, Appl. Phys. Lett. **73**, 496 (1998).
[35] I. Shtrichman, D. Gershoni, and R. Kalish, Phys. Rev. B **56**, 1509 (1997).
[36] P. Michler, A. Hangleiter, M. Moser, M. Geiger, and F. Scholz, Phys. Rev. B **46**, 7280 (1992).
[37] J. Feldman, G. Peter, E. O. Gobel, P. Dawson, K. Moore, C. Foxon, and R. J. Elliot, Phys. Rev. B **59**, 2337 (1987).
[38] M. Colocci, M. Gurioli, and J. Martinez-Pastor, J. Phys. IV **3**, 3 (1993).
[39] L. C. Andreani, Solid State Commun. **77**, 641 (1991).
[40] R. Zimmermann and E. Runge, in *Physics of Semiconductors*, edited by D. J. Lockwood (World Scientific, Singapore, 1995), p. 1424.
[41] P. Lefebvre, J. Allegre, B. Gil, A. Kavokine, H. Mathieu, W. Kim, A. Salvador, A. Botchkarev, and H. Morkoc, Phys. Rev. B **57**, R9447 (1998).
[42] E. O. Kane, in *Handbook in Semiconductors*, edited by W. Paul (North-Holland, Amsterdam, 1982), Vol. 1, pp. 193–217.
[43] G. L. Bir and G. E. Pikus, in *Symmetry and Strain-Induced Effects in Semiconductors* (Wiley, New York, 1974).
[44] M. Suzuki, T. Uenoyama, and A. Yanase, Phys. Rev. B **52**, 8132 (1995).
[45] S.-H. Park and S.-L. Chuang, Phys. Rev. B **59**, 4725 (1999).
[46] T. Yang, S. Nakajima, and S. Sakai, Jpn. J. Appl. Phys., Part 1 **34**, 5912 (1995).
[47] S. Wei and A. Zunger, Appl. Phys. Lett. **69**, 2719 (1996).
[48] M. D. McCluskey, C. G. Van de Walle, C. P. Master, L. T. Romano, and N. M. Johnson, Appl. Phys. Lett. **72**, 2725 (1998).
[49] L. Bellaiche, T. Mattila, L.-W. Wang, S.-H. Wei, and A. Zunger, Appl. Phys. Lett. **74**, 1842 (1999).